Time-of-flight measurement-based three-dimensional profiler system employing a lightweight Fresnel-type Risley prism scanner

Jae Heun Woo,a Chu-Shik Kang,a,b Jong-Ahn Kim,a Jae Wan Kim,a Sunghoon Eom,a and Jae Yong Leea,*

aKorea Research Institute of Standards and Science, Length Group,
Division of Physical Metrology, Daejeon, Republic of Korea
bKorea University of Science and Technology, Department of Science of Measurement,
Daejeon, Republic of Korea

Abstract. A time-of-flight measurement-based three-dimensional (3D) profiler system employing a lightweight scanning system is demonstrated. To reduce the weight of the scanning system, and thereby achieve faster scanning speeds, two Fresnel prism sheets were employed as the scanning optics and installed to work as a pair of Risley prisms. Each Fresnel prism sheet has a diameter of 102 mm and mass of 15 g, which is about 12 times lighter than ordinary bulky prism. By scanning the laser beam with the developed scanning system, a 3D point cloud image of a target object located 8 m away could be successfully obtained. The image distortion was removable by correcting six geometrical parameters of the scanner using a simple optimization algorithm. It was confirmed by the experiment that once the distortion has been corrected, it is valid for other scanning speeds (and trajectories), enabling 3D profile measurements that do not require postprocessing of measured data. Measurement results for a standard target composed of square extrusions were in good agreement with the reference values, with deviations of <1 mm.

1 Introduction

With the emergence of the fourth industrial revolution (Industry 4.0), one of the essential technologies is measuring instruments that can be used to gather three-dimensional (3D) information about distant objects. Optical 3D measurement systems based on active noncontact methods can be used in a wide variety of application areas because they are capable of fast, easy, and geometry-free measurements, and allow a tremendous number of data points compared with other contact methods.[1–3] Depending on the application field and measurement specifications, an optical 3D profiler requires a suitable working principle and design considerations appropriate for the measurement purposes.

Structured-light 3D scanning (also known as fringe projection profilometry)[4–6] is one of the popular 3D measurement techniques currently used in industrial applications. It can be used to measure the surface profiles of an object with high accuracy in the submillimeter range. However, the measurement distance is usually limited to a few meters because the light irradiation intensity is spread over fringe projection patterns, resulting in a low signal-to-noise ratio (SNR) of fringe detection.[7] In addition, the light signal scattered from distant objects can be very weak when received with an imaging aperture of limited size.

On-site measurement using a mobile 3D profiler system is desirable for medium-to-long distance ranges,[8] as the objects of interest to be measured are often too large to be carried into

---

*Address all correspondence to Jae Yong Lee, jaeyong@kriss.re.kr

a laboratory.[1] In this case, to achieve return signals with a sufficient level of SNR, it would be preferable, rather than relying on single-shot approaches, such as a flash light detection and ranging (LiDAR),[9] to combine a high-peak-power pulse light source and an optical beam scanning mechanism. Provided that the angular scanning of the light beam is fast and accurate, one can take advantage of time-of-flight (ToF) measurements using the high-SNR pulsed light backscattered from a distant object surface, point by point, which would then cover distances from medium (over 2 m) to long (up to 100 m) range. When implementing a mobile measuring system, compactness and light weight are relevant design factors to be considered.

This approach of point-scanning ToF measurement puts some specific demands on a light beam scanner, including a high frame rate, efficient signal collection, and large field-of-view (FOV). When using a beam scanner involving mechanical motion, light weight and mechanically robust moving components are crucial to measurement speed and achievable accuracy.[10–12]

Many recent efforts have explored plate-type or inertia-free scanning components, such as polarization gratings, Fresnel lenses, planar phase-shifting surfaces, and so on.[11,13–19] Each has demonstrated its own benefits in terms of device weight, scanning speed, beam steering range, beam aperture size, and so on. They provide potential advantages by reducing the size and weight of the beam steering mechanisms. However, while these devices have the sophisticated design and control necessary to carry out the desired beam steering,[11,13] they suffer from complicated setup geometries, which are needed to accommodate the optical paths of both the transmission and return beams.[16] Further investigations are still on going to address the technical challenges of measurement capability and flexibility, such as steering angle range, scanning trajectory, density of scanning points, etc.[18,19]

Recently, a beam steering mechanism that is simple in working principle with robust mechanical motion, the "Risley prism (RP)" configuration, came to our attention. An RP,[20–22] consisting of a set of two identical wedge prisms whose individual orientations can be arbitrarily set. RPs are well known as a versatile two-dimensional (2D) angular beam positioner. The rotational motions of its components greatly reduce the mechanical burden required for fast oscillatory motions of a galvanometer scan system.[23] It is also straightforward to configure the scanning trajectory and speed of the 2D beam steering of an RP system using a few control parameters, such as the rotation velocities and initial angular phases of the two prism components, given their wedge angles.[21] However, when attempts have been made to increase the scanning speed of an RP system, the render rotations of the bulky wedge prisms become vulnerable to mechanical "wobbling" due to the weight imbalance of the prisms. This is even more troublesome for an RP scanner with greater wedge angles and/or a larger aperture size.[13,24]

Here, we suggest using thin, lightweight Fresnel prism sheets instead of bulky wedge prisms, to resolve these inherent difficulties, which impose critical restrictions on the implementation of a fast RP scanner-assisted ToF ranging, with large FOV, and efficient signal collection. The idea of introducing Fresnel optics to reduce the weight of a large-aperture light scanner dates back to the early 1970s and their use in space optics.[23] A similar approach has been widespread in the field of laser endoscopy, where utmost scanning speed is pursued with miniaturized RPs only a few millimeters in size.[24]

In this paper, a suitable implementation of a Fresnel-type RP scanner is revisited, specifically for the development of a fast laser-scanning 3D surface profiler based on medium-to-long range ToF measurements. It has the advantages of excellent weight balance as well as large aperture size, which is readily available with commercial Fresnel prism sheets. Operating a Fresnel-type RP scanner with a sufficient level of dimensional accuracy requires not only good mechanical agility and robustness but also precisely aligned assembly and the components. Each separate prism sheet sits properly on a hollow-shaft motorized stage and needs to rotate coaxially, coinciding with the optical axis of a Fresnel-type RP system, which is preferably determined by the direction of an incident laser beam. The actual beam steering achieved by the RP system cannot be evaluated exactly using a simple geometrical model,[20] which can cause erroneous prediction of the beam deflection angles, which might, in turn, lead to appreciable distortion in the measured 3D profiles. A proper method is required to characterize the scanner alignment errors and correct the misleading dimensional information contained in the 3D scanned data.

We began with a theoretical formulation to model the geometrical optics involved with a Fresnel-type RP system, taking into account the system parameters relevant to both the

Fresnel prism sheet itself (such as the prism wedge angle, thickness, and refractive index) and additional concerns with its initial operating conditions (the rotation angles of the RP components) as well as with the mechanical assembly (the gap between the prism sheets and orientational misalignments of the rotation axis of individual prisms). Once built, we then utilized our formulation to experimentally determine the key parameters of a Fresnel-type RP system, which can then readily serve as its accurate beam scanning model.

In the experiment, we developed a 3D surface profiler based on pulsed-laser ToF sensing that combines a Fresnel-type RP scanner with an aperture diameter of 80 mm. The laser beam was fast scanned transversely over an object surface, and the backscattered signals were collected and descanned using the same scanner concomitantly. Using a standard target consisting of several square extrusions of 10-mm step height, we acquired 3D point cloud data and applied our Fresnel-type RP scanning model to accomplish the best fit between the experimental result and the ideal dimensional features of the standard target.

We describe numerical details about how to determine the actual scanner parameters and show the consequence of this scanner correction, which affects the transverse coordinates of the scanning 3D ToF measurements. We demonstrate the feasibility of our idea, which improved dimensional accuracy of the reconstructed 3D profiles successfully.

2 Principle of Laser-Scanning ToF Measurement Using a Fresnel-Type Risley Prism Scanner

A 3D profile measurement systems using scanning mechanisms usually consists of a light source, a transmitter part including a scanning system, and a receiver part containing a detector system. Figure 1 shows a schematic diagram of a typical scanning-type 3D profile measurement system. A pulsed laser beam is scanned over the object surface, and the 3D coordinates of each object point are obtained using the ToF distance and the beam steering angle, which are measured simultaneously. The ToF distance r_{ToF} refers to the distance between the scanner and the target point excluding the offset distance between the photodiodes and the scanner. In Fig. 1, the 3D coordinates of object point P_{sample} are represented by a transverse component $d_\perp$, which can be expressed as $\sqrt{x^2 + y^2}$ and a z component L_z.
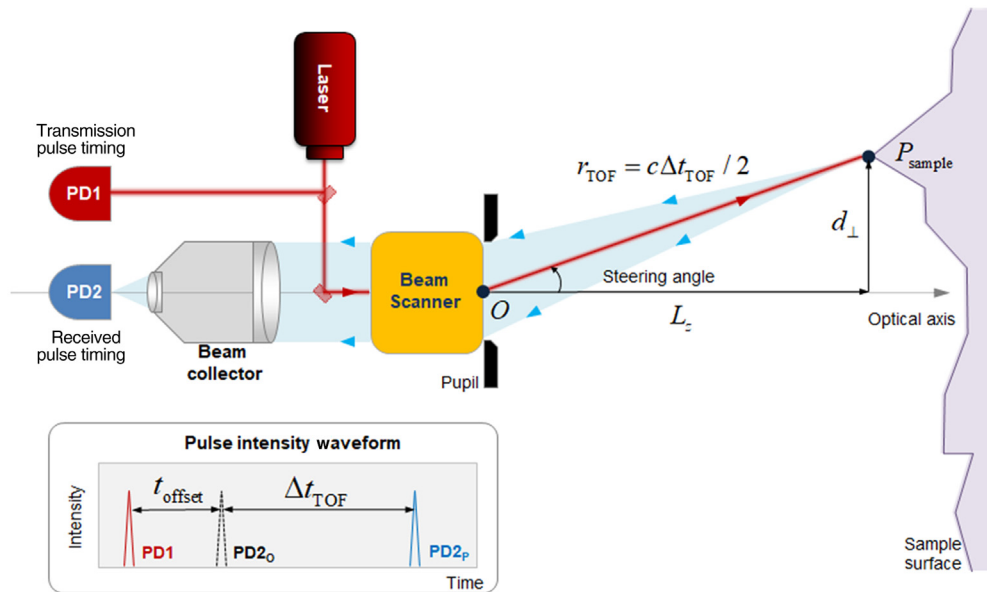
Fig. 1 Schematics of a scanning-type 3D profile measurement system. r_{TOF}: distance between the scanner and the target point; c: speed of light; Δt_{ToF}: time of flight; $d_\perp$: transverse component of object point P_{sample}; L_z: z component of object point P_{sample}.

In the proposed measurement system, a Fresnel-type RP that consists of two Fresnel wedge prisms is used as the scanner optics. Thus, the beam steering angle becomes a function of the parameters of the two rotating prisms, which include refractive indices, wedge opening angles, and rotating angles.

2.1 Ray Tracing of an Optical Beam Steered by a Risley Prism Scanner

Figure 2 shows a schematic diagram of an RP scanner consisting of two wedge prisms. The real Risley scanner used in this work is composed of two Fresnel prism sheets; but for better visualization of the parameters used in the calculations, two bulky wedge prisms are shown instead here. The origin of the coordinate system, O, is located on the fourth surface [4 in Fig. 2(a)] of the RP. The second and third surfaces [2 and 3 in Fig. 2(a)] are parallel to each other and perpendicular to the z axis.

The unit normal vector of each prism surface is denoted as $\hat{s}_i$ ($i = 1, 2, 3, 4$). If the polar angle of each surface normal vector in the spherical coordinate system is denoted as $\theta_i (i = 1, 2, 3, 4)$, the wedge opening angle of each prism is determined as $\theta_{w1} = \theta_1 - \theta_2$ and $\theta_{w2} = \theta_4 - \theta_3$.

When the rotation angles around the z axis of the first and second prisms are ϕ_1 and ϕ_2, respectively, the unit normal vectors of the four surfaces of an RP can be expressed in Eq. (1) as
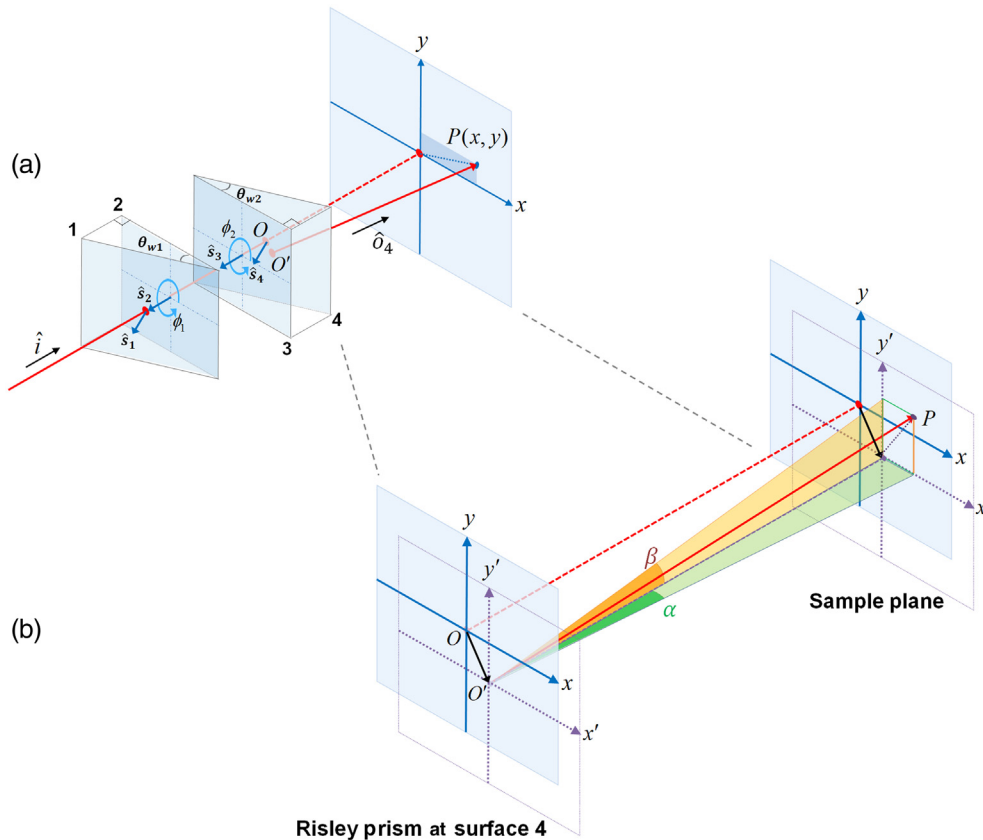
Fig. 2 (a) Schematic diagram of an RP scanner composed of two rotating wedge prisms. $\hat{i}$: direction vector of incident beam; $\hat{s}_1, \hat{s}_2, \hat{s}_3, \hat{s}_4$: surface normal vectors; θ_{w1}, θ_{w2}: wedge opening angles of the two prisms; ϕ_1, ϕ_2: rotation angles of two prisms around the z axis; $\hat{o}_4$: direction vector of the deflected output beam; O: origin of the coordinate system; and O': point through which the beam exits the RP. (b) Zoomed-in view of the last surface of RP and the sample plane. α and β are the angles between the z axis and projections of the direction vector $\hat{o}_4$ onto the xz plane and yz plane, respectively.

$$\hat{s}_1 = (\sin\theta_1 \cos\phi_1, \ \sin\theta_1 \sin\phi_1, \ \cos\theta_1),$$
$$\hat{s}_2 = (\sin\theta_2 \cos\phi_1, \ \sin\theta_2 \sin\phi_1, \ \cos\theta_2),$$
$$\hat{s}_3 = (\sin\theta_3 \cos\phi_2, \ \sin\theta_3 \sin\phi_2, \ \cos\theta_3),$$
$$\hat{s}_4 = (\sin\theta_4 \cos\phi_2, \ \sin\theta_4 \sin\phi_2, \ \cos\theta_4). \tag{1}$$

The rotation angles $\phi_i (i = 1,2)$ can be expressed in terms of the initial angle, $\phi_{0,i}$, and the rotated angle, $\phi_{r,i}$, as $\phi_i = \phi_{0,i} + \phi_{r,i}$. If the i'th prism's angular frequency of rotation is ω_i, the rotation angle at time t can be expressed in Eq. (2) as

$$\phi_i = \phi_{0,i} + \phi_{r,i} = \phi_{0,i} + \omega_i t. \tag{2}$$

To minimize the initial deflection angle of the output beam before rotation, the two prisms were set upside down to each other as shown in Fig. 2(a).

When a laser beam traveling in the negative z axis direction is incident on an RP, the direction vector, $\hat{o}_i$ $(i = 1, \ldots, 4)$, of the refracted beam at the i'th surface of the RP, can be derived using the vector form of Snell's law in Eq. (3) as[20]

$$\hat{o}_1 = \frac{1}{n_1}[\hat{i} - (\hat{i} \cdot \hat{s}_1)\hat{s}_1] - \hat{s}_1\sqrt{1 - \frac{1}{n_1^2} + \frac{1}{n_1^2}(\hat{i} \cdot \hat{s}_1)^2},$$

$$\hat{o}_2 = n_1[\hat{o}_1 - (\hat{o}_1 \cdot \hat{s}_2)\hat{s}_2] - \hat{s}_2\sqrt{1 - n_1^2 + n_1^2(\hat{o}_1 \cdot \hat{s}_2)^2},$$

$$\hat{o}_3 = \frac{1}{n_2}[\hat{o}_2 - (\hat{o}_2 \cdot \hat{s}_3)\hat{s}_3] - \hat{s}_3\sqrt{1 - \frac{1}{n_2^2} + \frac{1}{n_2^2}(\hat{o}_2 \cdot \hat{s}_3)^2},$$

$$\hat{o}_4 = n_2[\hat{o}_3 - (\hat{o}_3 \cdot \hat{s}_4)\hat{s}_4] - \hat{s}_4\sqrt{1 - n_2^2 + n_2^2(\hat{o}_3 \cdot \hat{s}_4)^2}, \tag{3}$$

where n_1 and n_2 are the refractive indices of the first and second prisms, respectively, and $\hat{i} = (0,0,-1)$ is the direction vector of the incident beam. The vector components of $\hat{o}_i$ $(i = 1, 2, 3, 4)$ will be expressed as $(o_{ix}, o_{iy}, o_{iz}) = (o_{ix}, o_{iy}, -o_{iz}^*)$ based on the coordinate convention used in this paper.

Due to refraction, the incident beam with the direction vector $(0,0,-1)$ does not pass through the origin O, but through a point O', whose 3D coordinates are $(x_{\text{dev}}, y_{\text{dev}}, 0)$ (see Fig. 2).[25]

As mentioned in Sec. 2, the ToF distance, r_{TOF}, is measured with reference to O', and thus the 3D coordinates of the object point under measurement are determined in Eq. (4) as

$$x = x_{\text{dev}} + x_{\text{TOF}},$$
$$y = y_{\text{dev}} + y_{\text{TOF}},$$
$$z = z_{\text{TOF}}, \tag{4}$$

where x_{TOF}, y_{TOF}, and z_{TOF} are the x, y, and z coordinates of r_{TOF}, respectively, when the origin is set as O'.

As already described in Sec. 2, the ToF distance, r_{TOF}, between the fourth surface of the RP and the target point under measurement is obtained by measuring the time difference Δt_{TOF} in Eq. (5) as

$$r_{\text{TOF}} = \sqrt{x_{\text{TOF}}^2 + y_{\text{TOF}}^2 + z_{\text{TOF}}^2},$$
$$= \frac{c\Delta t_{\text{TOF}}}{2}, \tag{5}$$

where c is the speed of light in air.

If we combine the information of r_{TOF} and the direction vector of the output beam, the 3D coordinates of the target point can be obtained as

$$
\begin{aligned}
x_{TOF} &= |z_{TOF}| \tan \alpha, \\
y_{TOF} &= |z_{TOF}| \tan \beta, \\
z_{TOF} &= -\frac{r_{TOF}}{\sqrt{1 + \tan^2 \alpha + \tan^2 \beta}},
\end{aligned}
\tag{6}
$$

where α and β are the angles between the z axis and projections of the direction vector $\hat{o}_4$ onto the xz plane and yz plane, respectively [see Fig. 2(b)].

By expressing α and β in terms of the direction vector components using the relations:

$$
\begin{aligned}
\tan \alpha &= o_{4x}/o_{4z}^*, \\
\tan \beta &= o_{4y}/o_{4z}^*,
\end{aligned}
\tag{7}
$$

Equation (6) can be rewritten as

$$
\begin{aligned}
x_{TOF} &= |z_{TOF}| \frac{o_{4x}}{o_{4z}^*}, \\
y_{TOF} &= |z_{TOF}| \frac{o_{4y}}{o_{4z}^*}, \\
z_{TOF} &= -\frac{r_{TOF}}{\sqrt{1 + \left(\frac{o_{4x}}{o_{4z}^*}\right)^2 + \left(\frac{o_{4y}}{o_{4z}^*}\right)^2}}.
\end{aligned}
\tag{8}
$$

On the other hand, (x_{dev}, y_{dev}), the x and y coordinates of the point O' can be obtained with Snell's law as Eq. (9), using the thickness of each prism sheet and the distance between the two prisms

$$
\begin{aligned}
x_{dev} &= D_1 \frac{o_{1x}}{o_{1z}^*} + D_{gap} \frac{o_{2x}}{o_{2z}^*} + D_2 \frac{o_{3x}}{o_{3z}^*}, \\
y_{dev} &= D_1 \frac{o_{1y}}{o_{1z}^*} + D_{gap} \frac{o_{2y}}{o_{2z}^*} + D_2 \frac{o_{3y}}{o_{3z}^*},
\end{aligned}
\tag{9}
$$
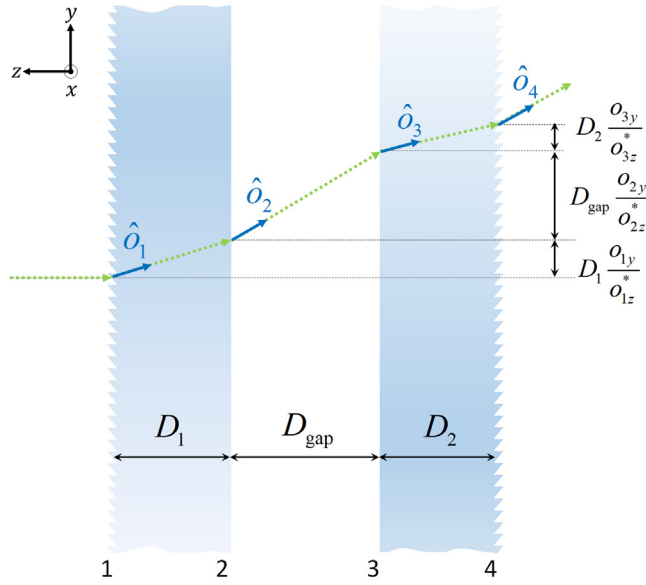
where D_1, D_{gap}, and D_2 are the distances between surfaces 1–2, 2–3, and 3–4, respectively, and o_{ix} and o_{iy} are the x and y components of $\hat{o}_i$ ($i = 1,2,3,4$) (see Fig. 3).

Finally, the 3D coordinates of an object point scanned by an RP scanner are measured as

$$
\begin{aligned}
x &= |z_{TOF}| \frac{o_{4x}}{o_{4z}^*} + D_1 \frac{o_{1x}}{o_{1z}^*} + D_{gap} \frac{o_{2x}}{o_{2z}^*} + D_2 \frac{o_{3x}}{o_{3z}^*}, \\
y &= |z_{TOF}| \frac{o_{4y}}{o_{4z}^*} + D_1 \frac{o_{1y}}{o_{1z}^*} + D_{gap} \frac{o_{2y}}{o_{2z}^*} + D_2 \frac{o_{3y}}{o_{3z}^*}, \\
z &= -\frac{r_{TOF}}{\sqrt{1 + \left(\frac{o_{4x}}{o_{4z}^*}\right)^2 + \left(\frac{o_{4y}}{o_{4z}^*}\right)^2}}.
\end{aligned}
\tag{10}
$$

2.2 Modeling Errors in Beam Direction Vectors Caused by Misalignment of the Scanner Prisms

Equation (10) shows how the 3D coordinates of the beam on the object could be measured using the information of the ToF distance and the direction vector of the output beam. This equation, however, is valid only when the scanning optics are perfectly aligned. In real measurements, perfect alignment is impossible and this will cause image distortion in the measured 3D profile, which needs to be corrected. There have been a number of studies to correct the distortion of

Fig. 3 Ray tracing of a beam propagating through the Fresnel prism sheets. D_1, D_{gap}, and D_2 are the distances between surfaces 1–2, 2–3, and 3–4, respectively, $\hat{o}_i$ (i = 1, 2, 3, 4) denotes the direction vector of the refracted beam at each interface. For simple visualization, the beam is assumed to be refracted in the yz plane.

images obtained using an RP scanner.[25,26] In this study, two correction factors that have major effects on the image distortion were considered. The two correction factors are the angular alignment error of the prism sheets and the initial angle difference, ϕ_0, between the two Fresnel prism sheets.

To mathematically manage the alignment errors of the prism sheets around the x and y axes, the rotation matrices shown in Eq. (11) were applied to Eq. (1) as shown in Eq. (12)

$$
\mathbf{R}_{x1} = \begin{pmatrix} 1 & 0 & 0 \\ 0 & \cos \delta_{x1} & -\sin \delta_{x1} \\ 0 & \sin \delta_{x1} & \cos \delta_{x1} \end{pmatrix}, \quad \mathbf{R}_{x2} = \begin{pmatrix} 1 & 0 & 0 \\ 0 & \cos \delta_{x2} & -\sin \delta_{x2} \\ 0 & \sin \delta_{x2} & \cos \delta_{x2} \end{pmatrix},
$$

$$
\mathbf{R}_{y1} = \begin{pmatrix} \cos \delta_{y1} & 0 & \sin \delta_{y1} \\ 0 & 1 & 0 \\ -\sin \delta_{y1} & 0 & \cos \delta_{y1} \end{pmatrix}, \quad \mathbf{R}_{y2} = \begin{pmatrix} \cos \delta_{y2} & 0 & \sin \delta_{y2} \\ 0 & 1 & 0 \\ -\sin \delta_{y2} & 0 & \cos \delta_{y2} \end{pmatrix}, \tag{11}
$$

and

$$
\begin{aligned}
\hat{e}_1 &= \mathbf{R}_{y1}\mathbf{R}_{x1}\hat{s}_1, \\
\hat{e}_2 &= \mathbf{R}_{y1}\mathbf{R}_{x1}\hat{s}_2, \\
\hat{e}_3 &= \mathbf{R}_{y2}\mathbf{R}_{x2}\hat{s}_3, \\
\hat{e}_4 &= \mathbf{R}_{y2}\mathbf{R}_{x2}\hat{s}_4.
\end{aligned} \tag{12}
$$

In Eq. (11), δ_{xi} and δ_{yi} (i = 1, 2) denote the pitch angle around the x axis and the yaw angle around the y axis of the i'th Fresnel prism sheet, respectively. Equation (12) shows the surface normal vectors of the two prism sheets when the prisms are slightly rotated around the x and y axes, due to misalignments.

Considering the alignment error of the Fresnel prism sheets, the beam direction vectors at the prism surfaces can be expressed as

$$\hat{o}_1 = \frac{1}{n_1}[\hat{i} - (\hat{i} \cdot \hat{e}_1)\hat{e}_1] - \hat{e}_1 \sqrt{1 - \frac{1}{n_1^2} + \frac{1}{n_1^2}(\hat{i} \cdot \hat{e}_1)^2},$$

$$\hat{o}_2 = n_1[\hat{o}_1 - (\hat{o}_1 \cdot \hat{e}_2)\hat{e}_2] - \hat{e}_2 \sqrt{1 - n_1^2 + n_1^2(\hat{o}_1 \cdot \hat{e}_2)^2},$$

$$\hat{o}_3 = \frac{1}{n_2}[\hat{o}_2 - (\hat{o}_2 \cdot \hat{e}_3)\hat{e}_3] - \hat{e}_3 \sqrt{1 - \frac{1}{n_2^2} + \frac{1}{n_2^2}(\hat{o}_2 \cdot \hat{e}_3)^2},$$

$$\hat{o}_4 = n_2[\hat{o}_3 - (\hat{o}_3 \cdot \hat{e}_4)\hat{e}_4] - \hat{e}_4 \sqrt{1 - n_2^2 + n_2^2(\hat{o}_3 \cdot \hat{e}_4)^2}. \tag{13}$$

The direction vector obtained using Eq. (13) should be used in Eq. (10).

The initial rotation angles of the two prism sheets, $\phi_{1,0}$ and $\phi_{2,0}$, are also important factors when determining the scanned beam positions. As the rotated angle of each Fresnel prism sheet is obtained from the readout of a rotary encoder, each Fresnel prism sheet, when the nominal values of $\phi_{1,0}$ and $\phi_{2,0}$ are both zero, should be precisely aligned so that its groove direction is exactly parallel to the y axis when the rotary encoder readout is zero. However, this is practically impossible, and angular alignment error may exist. Thus, the corrected initial angles of the two Fresnel prism sheets shown in Eq. (14) should be used to calculate the beam direction vectors:

$$\phi_{i,\text{ini}} = \phi_{i,0} + \phi_{i,\text{cor}} \quad (i = 1,2), \tag{14}$$

where $\phi_{i,\text{ini}}$, $\phi_{i,0}$, and $\phi_{i,\text{cor}}$ are the corrected initial angle, the nominal initial angle, and the correction angle of the i'th prism sheet, respectively.

The pitch angle around the x axis, the yaw angle around the y axis, and the correction for the initial rotation angle error of a Fresnel prism sheet, i.e., δ_{1x}, δ_{1y}, δ_{2x}, δ_{2y}, $\phi_{1,\text{cor}}$, and $\phi_{2,\text{cor}}$, can be determined through an optimization process, which can be summarized as follows.

To optimize the six parameters mentioned above, a standard specimen having several extruded squares (to be described in more detail in Sec. 4.2) was measured with the proposed 3D profile measurement system, and the x and y coordinates of the points on the boundary of the rectangles were found. If we denote the x and y coordinates of the j'th point on the i'th line segment to be x_{ij} and y_{ij}, respectively, these points are fitted to a straight line defined by $a_i x + b_i y + c_i = 0$ $(i = 1, \ldots, n)$. Then, χ_i^2, the sum of squares of the vertical distances between the i'th fitted line and the corresponding data points (x_{ij}, y_{ij}) are calculated over all line segments. The cost function of the optimization, χ^2, is the sum of χ_i^2 over all line segments, as shown in Eq. (15)

$$\chi^2 = \sum_{i=1}^{n} \chi_i^2 = \sum_{i=1}^{n} \sum_{j=1}^{m_i} \frac{(a_i x_{ij} + b_i y_{ij} + c_i)^2}{a_i^2 + b_i^2}, \tag{15}$$

where n is the number of line segments used for the optimization, and m_i is the number of data points on the i'th line segment. The values of the aforementioned six parameters are tuned until the minimum value cost function is obtained. Actual application results of the optimization are given in Sec. 4.

3 Setup of the Laser-Scanning ToF-Based 3D Profile Measurement System Using a Fresnel-Type Risley Prism Scanner

To verify the performance of the Fresnel prism sheets as lightweight scanning optics, Fresnel prism sheets were employed as scanning optics in the RP scanner.

Figure 4 shows a schematic diagram of the experimental setup of the 3D profile measurement system including the Fresnel-type RP scanner. A pulsed laser at a wavelength of 532 nm, with a repetition rate of 50 kHz and pulse width of 3 ns, was used as the light source. The average power was measured right after the intensity control component. The average power of the laser beam was controlled in the range between 25 and 40 mW. Beam diameter size was around 5 mm at the target plane. The distance to the target was located at around 8 m. A fast speed photodiode with a
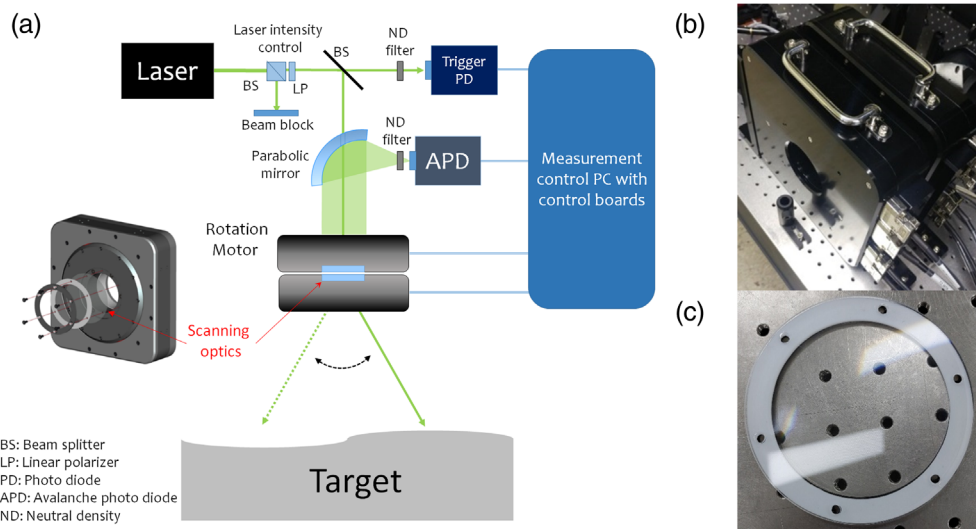
Fig. 4 (a) Schematic diagram of the 3D profile measurement system with the Fresnel-type RP scanner. (b) Photograph of the Fresnel-type RP scanning system. (c) Photograph of a mounted Fresnel prism sheet.

2-GHz bandwidth was used to detect the trigger pulse, and the return pulse from the target was collected by a parabolic mirror and focused to a fast speed avalanche photodiode with 1-GHz bandwidth. To control the rotation angles of the Fresnel prism sheets, two hollow-shaft torque motors equipped with a rotary encoder were used. The maximum rotation speed of the torque motors was 1000 revolutions per minute, and the positioning uncertainty of the rotary encoder was about 5.0″. The signal resolution of the rotary encoder was 72,000 counts per revolution. The diameter of the hollow hole was 80 mm, which becomes the aperture of the scanning optics.

When the trigger signal is detected by the trigger photodiode, the synchronized measurement system starts to measure the ToF signal. The distance to a target object is obtained from the ToF measurement of the pulsed laser, where the detection of the pulsed signal is performed using full-waveform-digitization.[27] The waveforms of the laser pulses were digitized with a sampling rate of 2.5 GHz using a 10-bit digitizer having a bandwidth of 1.5 GHz. The full waveform of the short pulse signal was measured, and the ToF between the trigger pulse and the return pulse was obtained after signal processing utilizing a Savitzky–Golay filter.[28] To find the peak positions of each pulse, the center-of-gravity (COG) method was applied to the data points in the waveform where the signal amplitude was above a threshold-level.

The RP scanning system consisted of two commercially available Fresnel prism sheets (Knight Optical Ltd., Part No. PFA12133) cut into the size of the rotation motor mount. Figure 4(c) shows a photograph of the Fresnel prism sheet made of polymethyl methacrylate (PMMA). It has a saw-tooth-like structure, with a 0.15-mm facet width and a prism opening angle of 24 deg, which gives a beam deflection angle of 12 deg. The thickness of each Fresnel prism sheet was 2 mm, and its mass was 15 g. The diameter of the cut Fresnel prism sheet was 102 mm, to give a clear aperture of 80 mm. A Fresnel prism sheet weighs only 1/12th that of an ordinary glass prism having the same wedge opening angle and aperture size.

4 3D Profile Measurement Employing the Fresnel-Type Risley Prism Scanner

4.1 *3D Point Cloud Generated by the 3D Profile Measurement System*

A preliminary measurement was performed using a simple target, as shown in Fig. 5(a). The target was composed of four tissue boxes, a foam board, and a bigger box, supported by a tripod. For indoor measurements, the scanning range has to be properly configured so that the scanning beam would not reach the ceiling or the floor of the laboratory. Among several scanning
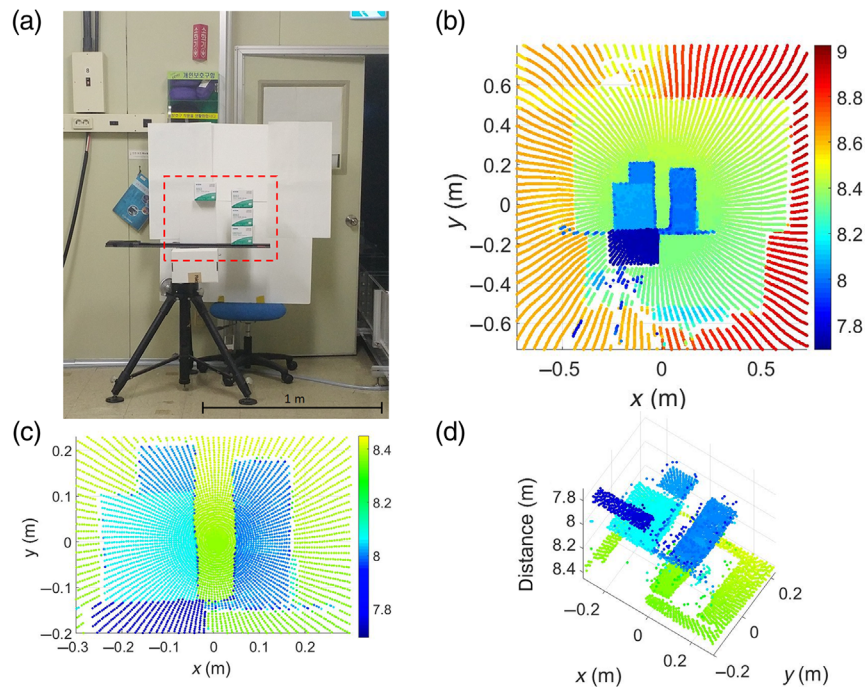
Fig. 5 Measurement target and its measured data. (a) Measurement target located 8 m from the measurement system. (b) A 3D point cloud image of the measurement target. Distance values are indicated by the color bar in meter unit. (c) A 3D point cloud image of the measurement targets in the red rectangle in (a). (d) Elevated view of (c).

trajectories that can be produced by the RP scanner, a spiral trajectory was employed that can be controlled to start scanning at the center of the scanning trajectory and spread out from the starting point as the scanning proceeds. A proper scanning range was selected, taking into account the spatial condition of the laboratory.

The rotation speeds of the two motors were 200.00 revolutions per minute and 200.10 revolutions per minute, respectively. By selecting the wedge angle of the Fresnel prism sheets, the maximum scanning range of the RP scanner was designed to be ±24 deg, but a full range measurement was not required for the target under measurement.

Figure 5(b) shows the 3D point cloud data of the measurement target placed 8 m from the measurement system, when the range of scanned angle was about ±4.7 deg for both horizontal and vertical directions, to cover the target, which was slightly bigger than 1 m. There are some parts where distance data were not obtained. These correspond to the darkest areas of the target where absorption of light is high, and the return signal becomes very weak. We employed a commercial component using Fresnel prism sheets. To minimize the power loss of the measurement system, it would be necessary to design a Fresnel prism sheet as a blazed grating. Figures 5(c) and 5(d) show the 3D point cloud data of the target inside the red rectangle shown in Fig. 5(a). The z_{TOF} (z coordinate of r_{TOF}) of each point of the target measured can be delineated in 3D as shown in Fig. 5(d). The standard deviation of repeatedly measured distance obtained at a fixed target point without scanning was <4 mm.

At the edges of the measurement objects shown in the 3D point cloud image [Fig. 5(d)], some points appear with erroneous distance information; this can be found by comparing Figs. 5(a) and 5(d). These erroneous points originate from the limited sampling rate of the digitizer and the low intensity of return signals from the target edges. The digitizer's maximum sampling rate of 2.5 GHz allows a minimum temporal sampling of 0.4 ns, corresponding to a resolution of 6 cm in ToF distance. In the waveform of weak signals returning from the edges, because of its low signal amplitude, the number of data points above the threshold-level decreases. The small number of data points leads to a peak position error in the COG calculation, resulting in a ToF distance measurement error. This is the performance limitation of the measurement system at the moment.
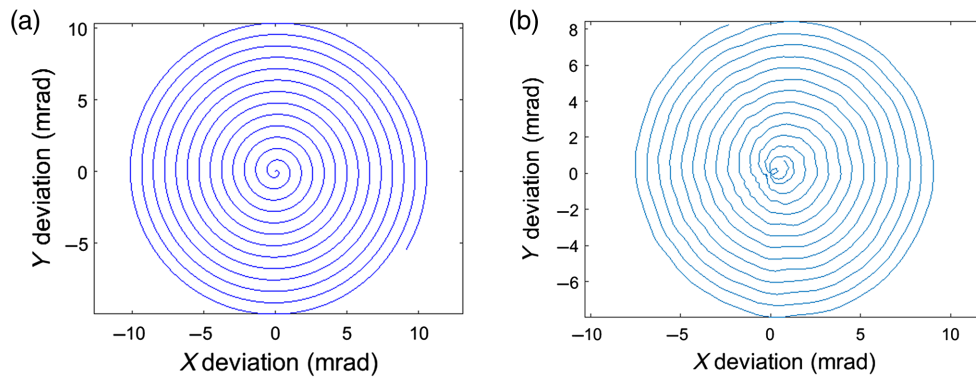
Fig. 6 Spiral scanning trajectories generated from: (a) theoretical simulation and (b) measured angle of the rotary encoder.

This edge measurement error may be overcome by employing a digitizer with higher sampling rate and by upgrading the signal processing algorithm.

In the measured 3D point cloud image, image distortion was especially found in the center part of the image, as shown in Fig. 5(c). Before performing a beam direction vector correction for the RP scanner, the experimental trajectory obtained from encoder output angle was checked.

Figure 6(a) shows the simulated data of a spiral scanning trajectory of ideal RPs, and Fig. 6(b) shows the calculated scanning trajectory measured from the rotary encoder angle of two hollow-shaft motors rotating at a speed of 200 revolutions per minute and 200.10 revolutions per minute, respectively.

The experimental scanning trajectory obtained by calculation using the measured angle data of the rotating motors differed from the theoretical trajectory, as shown in Fig. 6(b). This difference was more noticeable when the angular spacing between adjacent curves in the spiral trajectory was smaller, as shown in Figs. 7(a) and 7(c), where the two motors were rotating at the speed of 300 revolutions per minute and 300.01 revolutions per minute, respectively. The angular spacings are 0.80 and 0.04 mrad in Figs. 6(a) and 7(a), respectively.

For the theoretical trajectory, the difference in the rotation angles of the two scanning optics changes linearly in time [see Fig. 7(b)], but periodic fluctuations are observed in the experimental data, as shown in Fig. 7(d).

To confirm this effect, a periodic fluctuating component was added to the angle difference of the rotating scanning optics, and the theoretical scanning trajectory was calculated again. In the calculation, the angle difference fluctuation was modeled using a cosine function as shown in Eq. (16)

$$\Delta\phi(t) = \Delta\phi_0 + \Delta\phi_r + A\,\cos(\Omega_f t + \varphi_f), \tag{16}$$

where $\Delta\phi(t)$ is the rotation angle difference at time t, $\Delta\phi_0$ is the initial angle difference (at time $t = 0$), $\Delta\phi_r(t)$ is the relative angle difference at time t, A is the fluctuation amplitude, Ω_f is the frequency of fluctuation, and φ_f is the initial phase of the fluctuation.

When the scanning trajectory was calculated using the angle difference given in Eq. (16), a cleft shape was produced in the center of the theoretical scanning trajectory, as shown in Fig. 7(e). The major cause of the fluctuation in angle difference seems to be the eccentric error of the encoder scale or the first-order component of encoder scale error. This difference between the experimental and the theoretical trajectories of the scanning path itself does not add a measurement error to the 3D profile since the experimental scanning trajectory is the "actual" measurement trajectory. When one requires scanning trajectories to be implemented exactly as designed, such distorted trajectories in the actual experiment could be analyzed to inversely calculate the rotation angle of each scanning optic that can compensate for the distortion.[22]

Since the difference in scanning trajectory does not add distortion to the 3D point cloud image, the x and y coordinates obtained from the beam direction vector calculation of the RP scanner would be the major cause of 3D image distortion.
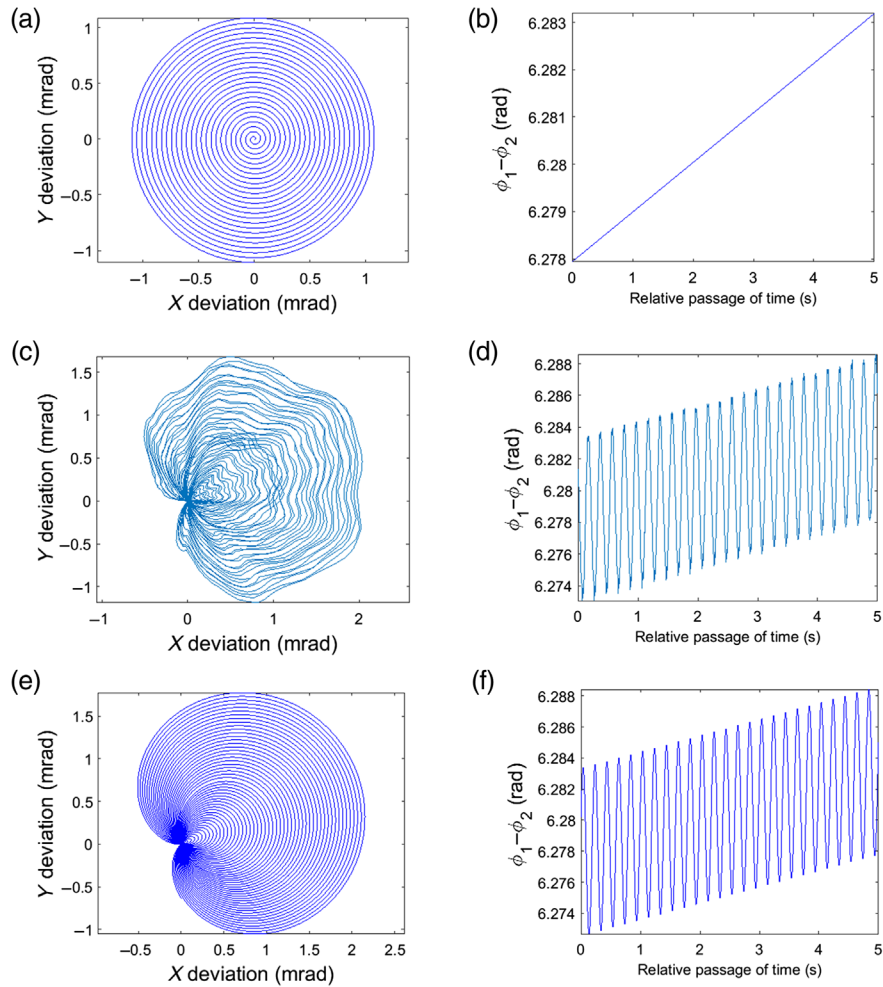
Fig. 7 Spiral scanning trajectory of the RP scanner system. (a) Theoretical calculation. (b) Theoretical rotation angle difference between two scanning optics. (c) Experimental scanning trajectory obtained from the measured rotation angles of the two scanning optics rotating at 300.00 revolutions per minute and 300.01 revolutions per minute, respectively. (d) Experimental rotation angle difference of the scanning trajectory shown in (c). (e) Theoretical trajectory obtained from rotation angle difference, including the modeled fluctuation component. (f) Theoretical difference in the rotation angle of the scanning trajectory shown in (e).

4.2 Experimental Correction of the Fresnel-Type Risley Prism Scanner Parameters

For evaluating the geometrical distortion of measured 3D images and correcting the scanner system parameters by the method outlined in Sec. 2.2, a standard target was designed and fabricated, referring to the target design introduced in Ref. 29. As shown in Fig. 8, the standard target has several square extrusion structures that can serve as a dimensional reference, utilizing their edge straightness, squareness of adjoining lines, and square width in both horizontal and vertical directions. There are square extrusion structures of two sizes with the same step height of 10 mm. The width of the large squares is 200 mm, whereas that of the small squares is 100 mm, with dimensional tolerances smaller than 0.07 mm over the entire specimen in all directions.

By applying the correction method to the measured 3D point cloud data, the actual values for the six geometrical parameters, $\phi_{1,\mathrm{corr}}$, $\phi_{2,\mathrm{corr}}$, δ_{x1}, δ_{y1}, δ_{x2}, and δ_{y2}, can be determined experimentally. The impact of distortion correction for the point cloud image on the dimensional accuracy of our 3D measurements can be evaluated by the comparison of geometrical aspects and dimensions measured with the reference values provided by the standard target.
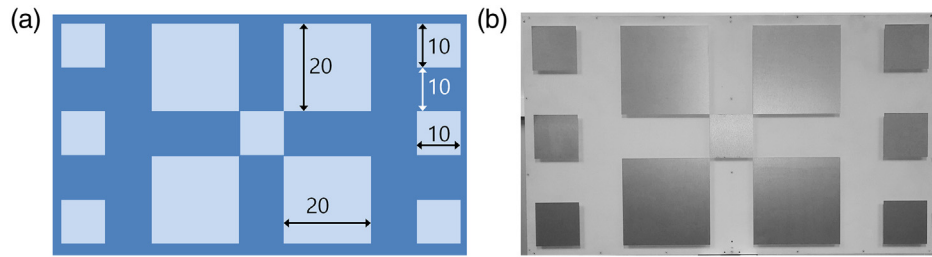
Fig. 8 The standard target. (a) Design layout of square extrusion structures (unit: cm). (b) Photograph of the standard target developed.

Figure 9 shows the 3D point cloud image of a portion of the standard target shown in Fig. 8. The rotation speeds of the two motors were set very closely, at 300.00 and 300.01 revolutions per minute so that the density of the point cloud of the image could be increased.[21] Compared with the photo of the standard target, its measured 3D point cloud image shows considerable distortion of the square features, as shown in Fig. 9(a).

The values for the six geometric parameters were searched using the optimization process described in Sec. 2.2. The values for the initial angle errors of the prisms, and the four tilt angles of the prism surfaces, were found to be $\phi_{1,\text{corr}} = -0.34$ deg, $\phi_{2,\text{corr}} = 0.23$ deg, $\delta_{x1} = 0.34$ deg, $\delta_{y1} = -0.45$ deg, $\delta_{x2} = -0.1$ deg, and $\delta_{y2} = -0.04$ deg, respectively.

By applying the optimized scanner system parameters found, the 3D image distortion was effectively corrected, as shown in Fig. 9(b). To evaluate the improvement in the dimensional accuracy of 3D reconstructed profiles, a more quantitative analysis on the width and step height of the square structures was performed. Before performing the dimensional analysis for the standard target, we numerically eliminated the inclination of the target surface through a least-squares 3D plane fitting to the point cloud data corresponding to the base plane around
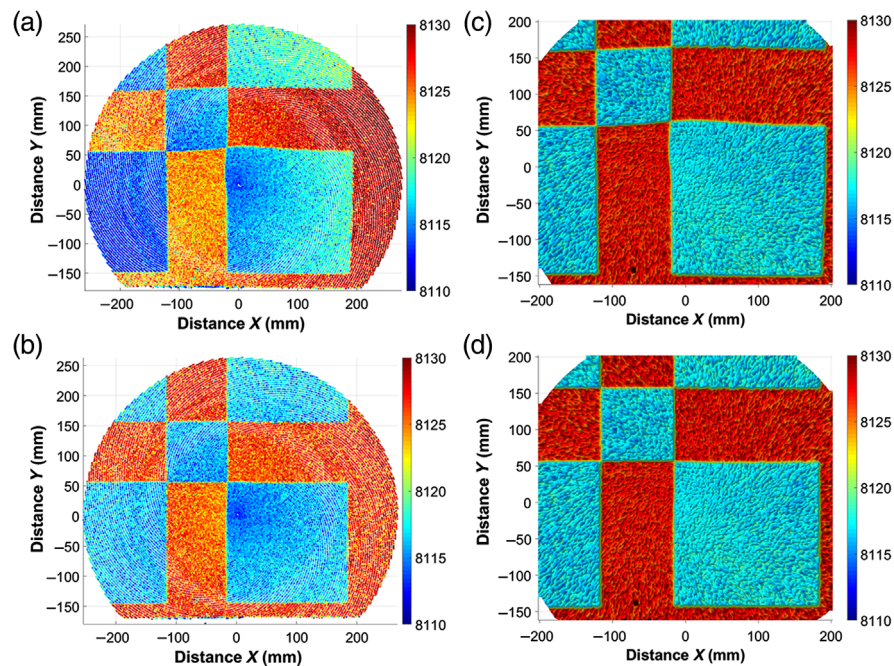
Fig. 9 Point cloud ToF data measured for the standard target (a) without any postprocessing and (b) after correction of the beam direction vectors of the scanner system, followed by a removal of sample plane inclination. Interpolated 3D profiles to have regular xy grids on the transverse plane (c) without and (d) with the scanner system correction, obtained from (a) and (b), respectively. In the graphics, z coordinate values (in the unit of mm) of ToF distance measurements are mapped in false colors, referring to the color bar on the right of each plot.
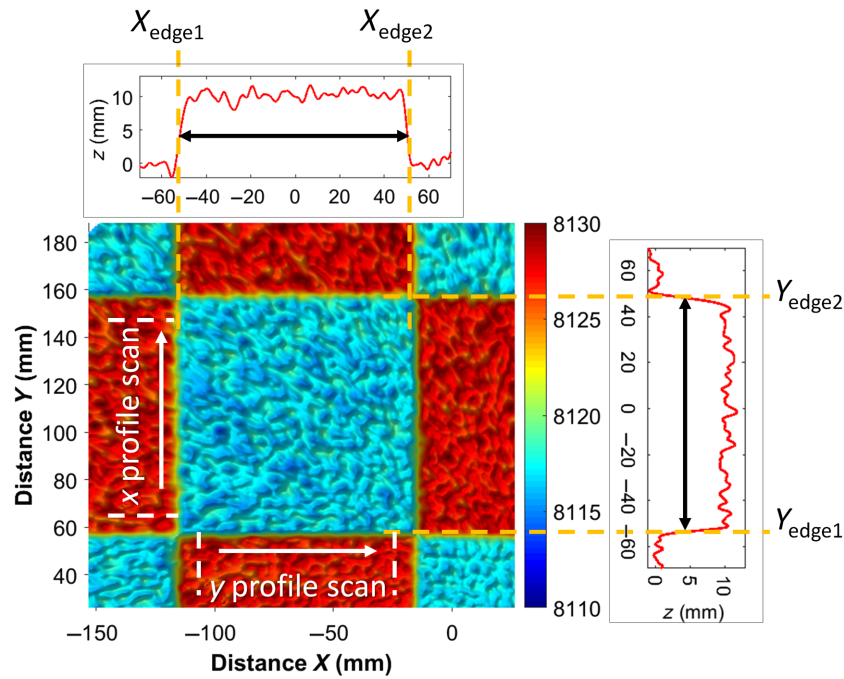
Fig. 10 Computational illustration of the 3D reconstructed profile cropped for cross-sectional profile analysis of the 100-mm square shown in Fig. 9(d). Top and right insets show the cross-sectional profiles across the square, taken in the x and y directions, respectively. To perform a cross-sectional analysis over the whole square, a cross-sectioning line is swept along its perpendicular direction as indicated by white arrows.

the extruded squares. Inclination angles of the base plane were evaluated to be 0.7 deg to the x axis and 0.3 deg to the y axis, and removal of the inclination made the normal vector of the base plane parallel to the optical axis of our scanner system. Thus, as can be seen in Fig. 9(b), the z_{TOF} (z coordinate of r_{TOF}) values of 3D point cloud data of the base plane are nominally equal. We then, for convenience in handling the data, interpolated such 3D point cloud data, each point indicated as (x_{TOF}, y_{TOF}, z_{TOF}), into a 3D reconstructed profile $z_{Profile}$ as function of 2D regular grid points (x_{RG}, y_{RG}) with a grid spacing of 0.1 mm for both for the x and y directions. Dimensional analysis for the 3D reconstructed profiles shown in Figs. 9(c) and 9(d) was carried out systematically for the two square targets with different sizes of 100 and 200 mm.

Figure 10 shows an illustration of how cross-sectional profiles were obtained from a 3D reconstructed profile cropped from the measured data given in Fig. 9, e.g., in the region containing the small (100 mm) square feature in Fig. 9(d). Applying a Gaussian filter with a radius of 2 mm, we obtained a smoothed 3D reconstructed profile within the region of interest to mitigate the difficulty involved with excessive spike noise in the following cross-sectional analysis. As displayed in the inset at the top (on the right) of Fig. 10, a cross-sectional profile across the square in the $x(y)$ direction has its step edges on both sides, located at X_{edge1} (Y_{edge1}) and X_{edge2} (Y_{edge2}), respectively. The edge positions of a cross-sectional profile were determined from the locations at which the profile's height value coincides with the precharacterized threshold value. Evaluating along the horizontal (vertical) line specified by $y = y_S$ ($x = x_S$), where the subscript S stands for scanning position, the separation between the two edges $X_{edge2} - X_{edge1}$ ($Y_{edge2} - Y_{edge1}$) in a cross-sectional profile was taken as the width D_X (D_Y) of the square. On the other hand, the step height was evaluated by averaging the height of the central part of the profile covering about 70% of the square width.

Detection of the edge positions was repeatedly performed while sweeping the profile under analysis in a direction perpendicular to the profile along the width of the square. For example, the X_{edge1} and X_{edge2} positions were obtained by sweeping the profile under analysis in the y direction [as depicted by the white arrow marked x profile scan in Fig. 10]. The obtained edge positions of the 100-mm square are plotted in Figs. 11(a), 11(b), 11(d), and 11(e).
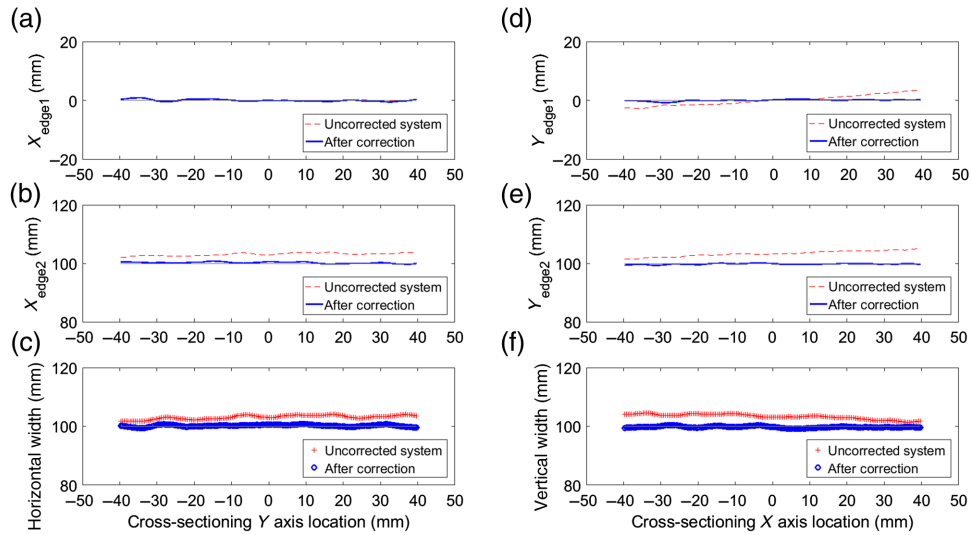
Fig. 11 Results of dimensional analysis performed on the 100-mm square. Geometrical features in the horizontal direction for the position of (a) left edges and (b) right edges, and (c) the resulting horizontal widths, evaluated on the cross-sectioning line swept inside the square along the *y* direction. Geometrical features in the vertical direction for the position of (d) bottom edges and (e) top edges, and (f) the resulting vertical widths, evaluated on the cross-sectioning line swept inside the square along the *x* direction.

To avoid interference from neighboring square structures, the edge position analysis was performed on the inner part of the square, excluding 10 mm from all edges. Figures 11(c) and 11(f) show the measured horizontal and vertical widths of the 100-mm square, respectively.

The red dotted lines in Figs. 11(b), 11(d), and 11(e) have positive slope, which means that the edge positions X_{edge2}, Y_{edge1}, and Y_{edge2} increase as the cross-sectioning position increases. This can be visually confirmed in Fig. 9(c). By applying the beam direction vector correction, these slopes were effectively eliminated, as can be seen by the blue bold lines in Figs. 11(b), 11(d), and 11(e).

The evaluated square widths and step heights for two squares are summarized in Table 1. After the correction of the beam direction vector, the square width values matched well with the reference values of the standard target, confirming the effect of the correction method and good performance of our system. On the other hand, the step height values did not show notable change after the correction because the vertical distance to the object is rather insensitive to a tiny change in the beam direction vector, as can be figured out from Eq. (10).

The good agreement between the measured step heights and the reference values, showing differences <1 mm, indicates the suitable performance of the ToF measurement system.

Table 1 Comparison of measured widths and step heights of the square patterns shown in Fig. 9(d), obtained before and after correction. Average values and standard deviations are shown.

Nominal width of square (mm)	Direction of measurement	Measured width (mm)		Measured step height (mm)	
		Without correction	With correction	Without correction	With correction
100	Horizontal	103.1 ± 0.7	100.2 ± 0.3	10.3 ± 0.3	10.3 ± 0.3
	Vertical	103.3 ± 0.9	99.79 ± 0.3	10.3 ± 0.4	10.3 ± 0.4
200	Horizontal	210.7 ± 2.6	199.6 ± 0.6	9.85 ± 0.3	9.91 ± 0.3
	Vertical	209.9 ± 2.2	197.8 ± 0.5	9.87 ± 0.3	9.93 ± 0.3

Among the measured horizontal and vertical widths of the two squares, vertical width of the 200-mm square showed largest deviation from the reference value (see Table 1), but it is expected that this can be improved by further enhancing the correction algorithm. Since making an exact correction was not the focus of this paper, measurement system parameters such as magnification and intrinsic prism errors such as the structural error of the prism geometry and the refractive index error of the prism material were not included in the current correction method. These additional correction parameters can be included in the correction algorithm in future work to improve the measurement results.

Since the six parameters used in the correction algorithm are all related to the geometric configuration of the scanning system, it is expected that once the values for these parameters are found through the optimization process, they will remain valid for other measurements with different scanning conditions.

To verify this, a 3D profile measurement was performed with different scanning condition. Figure 12 was obtained with the two motors rotating at speeds of 800.00 and 800.05 revolutions per minute, respectively. In spite of the different scanning condition, the distortion was successfully removed using the same correction algorithm based on the values of aforementioned six error parameters. This means that if once the error parameters are evaluated, they apply to any other measurements regardless of the scanning condition. This allows our measurement system to realize a real-time measurement without any postprocessing process. Although the test condition was limited by the maximum rotational speed (800 revolutions per minute) of the motor used, it is expected that our correction method would also apply when motors with higher rotational speeds are used.

In case of the 3D measurement shown in Fig. 12, the line spacing of the scanning trajectory was 0.7 mm, because the ratio of rotational speeds of the two motors ($800.00/800.05 = 0.99994$) was very close to 1, and it took about 34 s for the full scanning. A faster measurement could be implemented by either increasing the average speed of the motors (by employing faster motors in our case) or increasing the line spacing of the scanning trajectory by decreasing the ratio of the motor speeds.
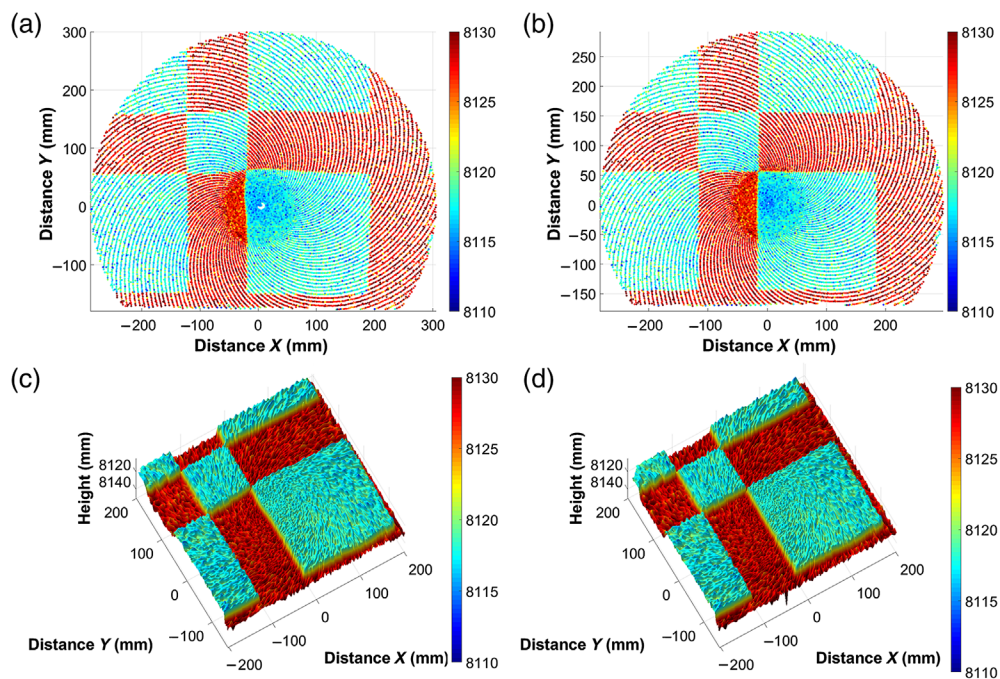
Fig. 12 Demonstration of scanning ToF measurements with high-speed operation of our Fresnel RP scanner (with the two prism sheets rotating at 800.00 and 800.05 revolutions per minute, respectively). Point cloud ToF images of the standard target (a) without and (b) with the scanner system correction, plotted after applying a tip–tilt removal of the sample plane inclination. (c) and (d) are the 3D surface profiles reconstructed from the point cloud data in (a) and (b), respectively.

The data acquisition rate also influences the measurement time and data density of the image. Figure 12 was obtained with a low data acquisition rate of 700 Hz, where the maximum spacing between data points along the scanning trajectory was 36 mm. Whereas the maximum data acquisition rate is 10 kHz in the present measurement system, it could be increased up to the laser repetition rate of 50 kHz if a high-performance acquisition system is used. For the measurement area shown in Fig. 12, if motors rotating with a speed of 5000 revolutions per minute are used with 10-kHz data acquisition rate, the maximum spacing between data points along the scanning trajectory would be 17 mm, which is similar to the case shown in Fig. 9. Therefore, using such a high-speed motor system, the area shown in Fig. 12 could be measured in 6 s, with the comparable image quality of Fig. 9. In addition, if the speed ratio of the two motors is set to 0.999 63, the line spacing of the scanning trajectory would be 4 mm (at a distance of 8 m), and the frame rate of one image per second could be achieved.

5 Conclusion

In conclusion, this study verified that the 3D profile of distant objects could be measured using a scanning system consisting of two Fresnel prism sheets that are substantially lightweight compared to conventional bulky prisms. Having a large wedge angle of 24 deg and a large aperture of 80 mm, Fresnel prism sheets allow high-speed rotation without wobbling that is usually experienced with bulky prisms resulting from weight imbalance. Distance measurement and 3D structural reconstruction performance were evaluated, confirming the validity of our system as a 3D profiler system. The proposed measurement system showed suitable performance, measuring a 3D structure located at a distance of 8 m. The measured values of square width and step height were in good agreement with reference values, with deviations of <1 mm.

The correction method for beam direction vector was clearly effective in correcting the distortion of the 3D image and can be further enhanced in future work to obtain more accurate results for 3D structural reconstruction with additional correction parameters. It was confirmed by the experiment that once the error factors have been evaluated for a given scanning condition, they can be applied to other conditions as well. Thus, after analyzing the measured data once using a simple optimization process, a real-time measurement of a 3D profile is possible without any post-processing of the measured data.

The frame rate in the present measurement was not high due to the dense scanning trajectory and the limited maximum rotation speed of the motor. Using Fresnel prism sheets rather than bulky prisms, rotational inertia was remarkably reduced, and the weight of the scanning optics was no longer a limiting factor of rotation speed. By employing a motor system with a faster rotation speed while controlling the line spacing of the scanning trajectory, the frame rate can be improved up to one image per second. Decreasing the weight of the scanning optics allows both faster rotation speed and higher frame rate. If the motor system allows higher rotation speed, a higher frame rate can be achieved by controlling the rotation speed of the motors, line spacing of the trajectory, and the spacing between data points along the scanning trajectory, considering the system parameters such as the probing beam size, target size, measurement distance, and so on, to achieve the desired image quality.

Using the Fresnel prism sheet as a lightweight scanning optics, the geometrical and mechanical limitations could be alleviated considerably, which is advantageous for mobile 3D scanning systems with a more compact design and faster scanning speed. We expect the Fresnel RP scanner configuration, presented in this study, to promise substantial benefits in developing a fast-scanning 3D profilometer with a wide FOV that works for measurement distances from medium (over 2 m) to long (up to 100 m) range.

Acknowledgments

References

1. R. H. Schmitt et al., "Advances in large-scale metrology—review and future trends," *CIRP Ann. Manuf. Technol.* **65**, 643–665 (2016).
2. R. Lange et al., "Time-of-flight range imaging with a custom solid state image sensor," *Proc. SPIE* **3823**, 180 (1999).
3. G. Rodger, D. Flack, and M. McCarthy, "A review of industrial capabilities to measure free-form surfaces," NPL Report, DEPC-EM 014 (2007).
4. K. Zhang et al., "3D reconstruction of complex spatial weld seam for autonomous welding by laser structured light scanning," *J. Manuf. Process.* **39**, 200–207 (2019).
5. W. Changwei, T. Ruiyin, and Z. Jing, "A survey of surface reconstruction techniques for line structured light systems," *J. Phys. Conf. Ser.* **1345**, 042053 (2019).
6. H. Yu et al., "Three-dimensional shape measurement technique for large-scale objects based on line structured light combined with industrial robot," *Optik* **202**, 163656 (2020).
7. E. Marti et al., "A review of sensor technologies for perception in automated driving," *IEEE Intell. Transp. Syst. Mag.* **11**, 94–108 (2019).
8. J. Beraldin, D. Mackinnon, and L. Cournoyer, "Metrological characterization of 3D imaging systems: progress report on standards developments," in *17th Int. Congr. Metrol.*, EDP Sciences, p. 13003 (2015).
9. G. M. Williams, Jr., "Optimization of eyesafe avalanche photodiode lidar for automobile safety and autonomous navigation systems," *Opt. Eng.* **56**(3), 031224 (2017).
10. V. Vuthea and H. Toshiyoshi, "A design of Risley scanner for LiDAR applications," in *Int. Conf. Opt. MEMS and Nanophotonics*, IEEE, Lausanne, pp. 1–2 (2018).
11. M. Bawart et al., "Dynamic beam-steering by a pair of rotating diffractive elements," *Opt. Commun.* **460**, 125071 (2020).
12. A. Li et al., "Risley-prism-based multi-beam scanning LiDAR for high-resolution three-dimensional imaging," *Opt. Lasers Eng.* **150**, 106836 (2022).
13. C. Oh et al., "A new beam steering concept: Risley gratings," *Proc. SPIE* **7466**, 74660J (2009).
14. M. U. Afzal, A. Lalbakhsh, and K. P. Esselle, "Electromagnetic-wave beam-scanning antenna using near-field rotatable graded-dielectric plates," *J. Appl. Phys.* **124**, 234901 (2018).
15. L. G. Cook and R. J. Withrington, "Method and laser beam directing system with rotatable diffraction gratings," US Patent 6,792,028 (2004).
16. C. Hoy et al., "Non-mechanical beam steering with polarization gratings: a review," *Crystals* **11**, 361 (2021).
17. N. Gagnon and A. Petosa, "Using rotatable planar phase shifting surfaces to steer a high-gain beam," *IEEE Trans. Antennas Propag.* **61**(6), 3086–3092 (2013).
18. X. Cao et al., "Lidar system based on lens assisted integrated beam steering," *Opt. Lett.* **45**, 5816–5819 (2020).
19. N. Dostart et al., "Serpentine optical phased arrays for scalable integrated photonic lidar beam steering," *Optica* **7**, 726–733 (2020).
20. Y. Lu et al., "Theoretical and experimental determination of steering mechanism for Risley prism systems," *Appl. Opt.* **52**, 1389 (2013).
21. Y. Lu et al., "Frame frequency prediction for Risley-prism-based imaging laser radar," *Appl. Opt.* **53**, 3556–3564 (2014).
22. A. Li et al., "Inverse solutions for a Risley prism scanner with iterative refinement by a forward solution," *Appl. Opt.* **54**, 9981–9989 (2015).
23. W. L. Wolfe, J. E. Harvey, and B. C. Platt, "Large-aperture wide-angle infrared scanning system," Arizona University Tucson Optical Sciences Center (1972).
24. L. M. Wurster et al., "Design and development of a miniaturized scanning probe," in *Student Conf. Med. Eng. Sci.: Proc.*, GRIN Verlag, Vol. 2, p. 63 (2013).
25. F. Huang et al., "Error analysis and optimization for Risley-prism imaging distortion correction," *Appl. Opt.* **60**, 2574–2582 (2021).
26. Y. Zhou et al., "Pointing error analysis of Risley-prism-based beam steering system," *Appl. Opt.* **53**, 5775 (2014).

27. C. Mallet and F. Bretar, "Full-waveform topographic lidar: state-of-the-art," *ISPRS J. Photogramm. Remote Sens.* **64**, 1–16 (2009).
28. W. Gander and J. Hrebicek, *Solving Problems in Scientific Computing Using Maple and MATLAB*®, 3rd ed., p. 135, Springer-Verlag, Berlin, Heidelberg (1997).
29. J. Hiremagalur et al., "Creating standards and specifications for the use of laser scanning in Caltrans projects," No. CA07-0964 (2007).

Jae Heun Woo received her PhD in chemistry and nanoscience from Ewha Woman's University, Seoul, Republic of Korea, in 2011. She is currently a senior research scientist at the Length Group, Division of Physical Metrology, Korea Research Institute of Standards and Science (KRISS). Her current research interests include dimensional metrology and large-scale and long-distance 3D measurement using light detection and ranging technology.

Chu-Shik Kang received his PhD in physics from Korea Advanced Institute of Science and Technology (KAIST), Daejeon, Republic of Korea, in 1993. He has been working at KRISS, Daejeon, Republic of Korea since 1994 and has been a professor at the University of Science and Technology, Daejeon, Republic of Korea since 2005. His research interests include high precision length measurements, dimensional metrology, and evaluation of measurement uncertainty.

Jong-Ahn Kim received his PhD in mechanical engineering from KAIST, Daejeon, Republic of Korea, in 2001. From 2001 to 2002, he worked as a principal researcher at Samsung Corning Micro-Optics in the Automation Group. After joining the KRISS in 2002, he developed several standard instruments for dimension metrology and has been interested in optical metrology based on interferometry and imaging processing.

Jae Wan Kim received his PhD in physics from KAIST, Daejeon, Republic of Korea, in 1999. In 1999, he joined KRISS, Daejeon. From 2009 to 2014, he led the Center for Length, KRISS. In KRISS, he was involved in a precision length metrology field. His current research interests include high-speed optical measurement and inspection.

Sunghoon Eom is a senior engineer at KRISS. He received his BS degree in electronic engineering from the University of Keimyung in 2010 and his MS degree in electronic engineering from the University of Hanyang in 2012. His current research interests include optical metrology and calibration systems.

Jae Yong Lee majored in physics and received his PhD from KAIST, Republic of Korea, in 2000. He has been working for KRISS as a principal research scientist since 2001. His research interests have evolved from ultrasensitive laser spectroscopy, photonic quantum computation, nonlinear optical microscopy, and super-resolution imaging to length and dimensional metrology, with an emphasis on optical instrumentations and measurement standards to meet ever-growing industrial demands.